

Molecular Quantum Control Algorithm Design by Reinforcement Learning

Anastasia Pipi,^{1,*} Xuecheng Tao^{†,2,*}, Prineha Narang^{‡,2,3} and David R. Leibrandt^{§1}

¹*Department of Physics and Astronomy, University of California,
Los Angeles (UCLA), California 90095, USA*

²*Division of Physical Sciences, College of Letters and Science,
University of California, Los Angeles (UCLA), California 90095, USA*

³*Electrical and Computer Engineering Department,
University of California, Los Angeles (UCLA), California, 90095, USA*

(Dated: October 22, 2024)

Abstract

Precision measurements of polyatomic molecules offer an unparalleled paradigm to probe physics beyond the Standard Model. The rich internal structure within these molecules makes them exquisite sensors for detecting fundamental symmetry violations, local position invariance, and dark matter. While trapping and control of diatomic and a few very simple polyatomic molecules have been experimentally demonstrated, leveraging the complex rovibrational structure of more general polyatomics demands the development of robust and efficient quantum control schemes. In this study, we present a general, reinforcement-learning-designed, quantum logic approach to prepare molecular ions in a single, pure quantum state. The reinforcement learning agent optimizes the pulse sequence, each followed by a projective measurement, and probabilistically manipulates the collapse of the quantum system to a single state. The performance of the control algorithm is numerically demonstrated in the case of a CaH^+ ion, with up to 96 thermally populated eigenstates and under the disturbance of environmental thermal radiation. We expect that the method developed, with physics-informed learning, will be directly implemented for quantum control of polyatomic molecular ions with densely populated structures, enabling new experimental tests of fundamental theories.

Emails: [†]xuechengtao@ucla.edu, [‡]prineha@ucla.edu, [§]leibrandt@ucla.edu.

* These two authors contributed equally.

Low-energy, high-precision measurements provide a powerful tool to explore fundamental physics beyond the Standard Model (BSM)[1, 2]. The rich internal energy-level structure of polyatomic molecules presents sensitive probes to test BSM hypotheses. For example, the frequencies of the inversion transitions in hydronium are used by astronomers to search for violation of local position invariance and would be sensitive to potential dark energy carriers[3]; a minuscule energy shift is predicted in molecular enantiomers as a result of parity violation [4] and awaits experimental observation [5]. However, high-fidelity control of molecules remains challenging, because the rovibrational levels are densely populated and the transition frequencies among those states commonly overlap each other. In fact, the preparation of the molecules into a single, pure state is a central yet non-trivial quantum control task[6, 7].

Several methods have been developed for state preparation, including sympathetic cooling [8, 9], photoassociation of cold atoms [10], optical cycling [11, 12], and quantum logic spectroscopy[13] (QLS). Among these, QLS stands out as a unique control scheme[14, 15], requiring no specific restrictions on the internal structure of the molecular ion and enabling non-destructive detection of molecular ion states. Prominent experiments [16–22] have demonstrated the ability to measure and manipulate the quantum states of simple diatomic ions with QLS. As the dimension of the state space of the molecule [23] increases, the same level of precision control demands the development of efficient and robust quantum control techniques beyond current capabilities.

In this *Article*, we establish and demonstrate reinforcement learning (RL) as a general, powerful, and flexible strategy for QLS-based control of the quantum states of trapped molecular ions. RL enhances decision-making by reinforcing actions based on feedback from interactions with the environment and has been previously applied in state engineering[24–27] and gate optimization [28, 29]. We show, that by leveraging the complete history of control pulses and measurement results, RL can be employed to design QLS control algorithms to obtain single quantum states with elevated efficiency and robustness. This, to the best of our knowledge, represents a significant advance in the field. Notably, the RL approach works without the assumption of distinguishable transitions that the previous control protocol relies on, opening possibilities in high-precision control of polyatomic molecular ions with complex energy-level structures.

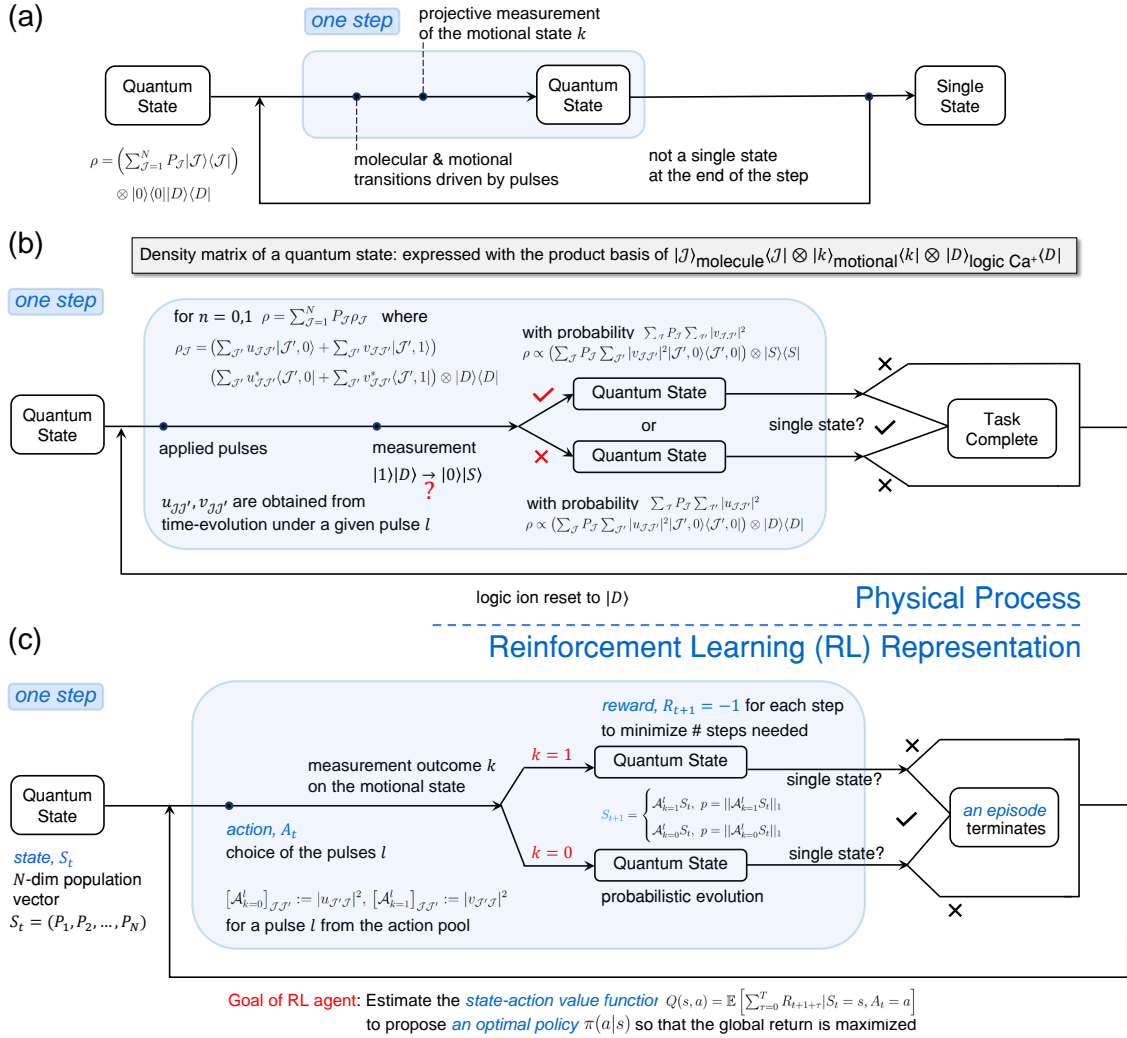


FIG. 1. (a) State preparation via projective measurements. A single quantum state is obtained by taking repetitive steps each consisting of two parts, namely, a laser pulse driving the motional sideband of a molecular state transition followed by a projective measurement of the motional state. (b-c) Detailed description of the two parts in a single step in the quantum logic spectroscopy experiments (b), and in the reinforcement learning framework (c). As shown in the schematic illustration, the evolution of the quantum state is tracked in terms of density matrices (b) and populations (c) during a single purification step. We assume that all coherence is destroyed in the motional state cooling leading to a diagonal density matrix.

We begin by introducing the QLS framework to prepare a single molecular state with projective measurements. For a simple molecular ion where the state transitions can be

uniquely distinguished, the protocol to prepare a single state with QLS was outlined[16] and experimentally demonstrated[16–19]. Initializing from a Boltzmann mixture of energetically accessible states ($|\mathcal{J}\rangle$), the protocol repeatedly drives blue-sideband transitions with selected pulses and performs projective measurements (using a quantum logic gate with a co-trapped logic ion) of the motional state (Fig. 1a). The projective measurement collapses the state to either the ground or excited motional state manifold according to the measurement result. As such, the associated population distribution of the molecular state, $P(\mathcal{J}) = \text{tr}(\rho|\mathcal{J}\rangle\langle\mathcal{J}|)$, is controlled, in a probabilistic manner, to collapse to a single, pure molecular state with probability above the purity threshold. The time evolution of the system throughout the process is illustrated in Fig. 1b with density matrices (Methods, Sec. A).

This state preparation framework is quite general, and large flexibilities appear in the choice of molecular transition to drive, or the optical pulses to apply. In previous work with CaH^+ [16–19], unique molecular transitions (under an external magnetic field with a specific field strength) were identified, and the pulse sequences were chosen to periodically sweep the possible transitions. This simple ‘sweeping’ strategy was experimentally demonstrated, however, it is expected to face difficulties for more complex molecular ions where transition frequencies often overlap. More importantly, the simplest sweeping protocol used in the first experiments does not take advantage of the historical measurement data, thus the number of pulses and measurements (i.e., the number of steps) needed to prepare a molecular state can be significantly optimized.

Reinforcement learning (RL) naturally emerges as the ideal approach for the state preparation task, by leveraging historical information to decide on the next action. The physical preparation process in Fig. 1b straightforwardly maps onto a sequential decision-making task, formalized as a Markov decision process in Fig. 1c. In the RL framework[30], the agent explores how a pulse sequence may potentially drive the system population and exploits the information from past attempts to guide current control decisions. The *state* of the system at time step t is tracked as an N_S -dimensional vector $S_t \in [0, 1]^{N_S}$, which represents the populations of the N_S accessible eigenstates. The RL agent selects a pulse l from the *action* library to apply at each step. The quantum-state evolution resulting from the selected pulse l is calculated using the time-dependent Schrödinger Equation and is inputted into the RL model as a set of transition matrices, \mathcal{A}^l (Fig. Extended 1 and Methods, Sec. B).

To account for the different measurement outcomes on the motional quanta, a different \mathcal{A}^l matrix is needed for each possible motional state in the projective measurement step. Taking both the coherent state evolution driven by laser pulses and the probabilistic wavefunction collapse during measurement together, the state-action dynamics are probabilistically determined and expressed as the four-argument function

$$p(S_{t+1}, R = r | S_t, l) = \|\mathcal{A}_k^l S_t\|_1, \text{ for } S_{t+1} = \mathcal{A}_k^l S_t, \quad (1)$$

with k the measurement outcome for the shared motional state ($k = 0, 1$), and $\|\cdot\|_1$ the 1-norm of the vector. Specifically, we do not distinguish $k > 1$ measurement results, and perfect measurement fidelity is assumed in the current study. The reward function R is set to a negative number, for example, $R = -1$ for each step regardless of the action taken to minimize the number of steps needed before a desired state is prepared, encouraging fast task completion. Overall, we expect the RL agent to learn the state-action value function, $Q(s, a)$, or the performance of the pulse sequences given the current quantum state. $Q(s, a)$ is expressed with a neural network that maps the population vector S_t to the action value, $Q(S_t, a)$, with $a = l$ the pulse choice from an action library of dimension N_A . In this work, we focus on the deep Q -learning algorithm[31–33] (for its exploration efficiency in the discrete action space, Methods [Sec. D](#)) with a simple, fully-connected network so that the operation time to evaluate the optimal pulse choice is shorter than the wall-clock pulse duration (~ 0.3 ms on a Nvidia 1080Ti GPU v.s. 1-100 ms pulses, for a typical problem size). The RL training and testing are performed with the PyTorch software package[34].

[Fig. 2](#) presents the usage of the reinforcement learning (RL) approach for state preparation. For illustration purposes, initially we consider only the low-lying $J \in 1, 2$ manifold of CaH^+ , described by the energy level diagram shown in [Fig. 2a](#). The laser pulses to drive the two-photon Raman transitions (dashed red arrows) for state preparation form the action library for RL simulations (pulses characteristics in [Table Extended 2](#) and the driven transitions in [Fig. Extended 2](#)). Previously, a similar pulse library was used at NIST[16] in the ‘sweeping’ protocol for state preparation; pulses in the library were sequentially and periodically applied to concentrate the population, followed by final projective measurement to obtain a single pure state. In contrast, here we choose to perform measurements after every molecular sideband pulse to obtain feedback on the instantaneous populations (see Methods, [Sec. C](#)). A sweeping protocol attempt is simulated in [Fig. Extended 3](#). Typically,

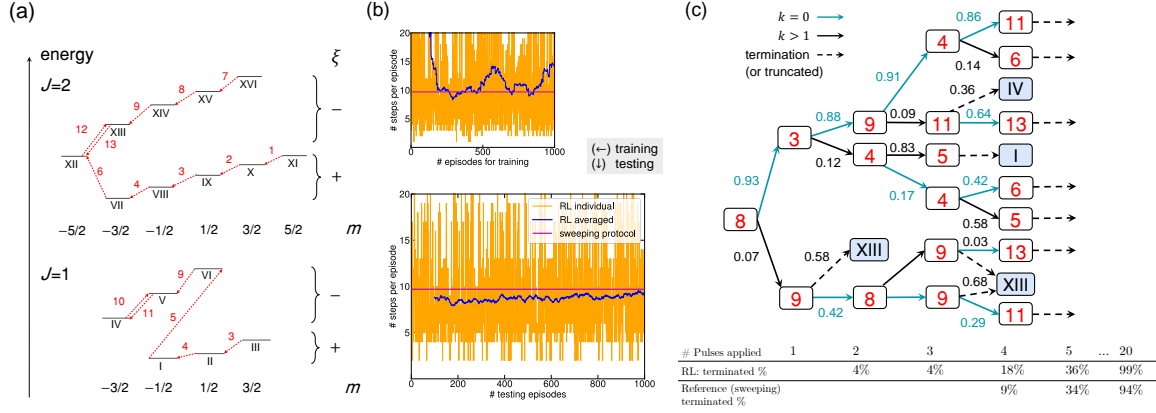


FIG. 2. (a) Partial energy level diagram of CaH^+ showing the low-lying rotational $J \in \{1, 2\}$ manifold, where an external magnetic field of 0.36 mT is applied to break the m degeneracy. A set of 13 uni-directional pulses (dashed red arrows) can be used to concentrate the population on the $|J, -J + 1/2, -\rangle$ states, followed by two pulses (bi-directional) to oscillate the population to the extreme state $|J, -J - 1/2, -\rangle$. The previous experiments [16] implemented a protocol that applies these laser pulses sequentially and repetitively for state purification (the ‘sweeping’ protocol). (b) The number of steps needed to prepare a pure molecular state with the reinforcement-learning (RL) designed protocol, for the case of CaH^+ ion. States in the $J \in \{1, 2\}$ rotational manifold (see Fig. 2) are occupied due to thermal excitation. Training and testing processes are presented separately. The average number of steps (solid blue) is obtained by averaging over the most recent 100 episodes. Five independent training/testing sessions get an average length of 8.7 under optimal hyperparameters. (c) A truncated decision tree of the RL-designed protocol. The complete version of the decision tree is shown in Fig. Extended 4. Pulse choices are reported in red numbers, and the terminal states (blue boxes, reached by dashed lines) are reported in Roman numerals. The branching probabilities are black and the color indicates the measurement outcome. The table reports the percentage of finished episodes with respect to the number of pulses applied. Computational details are reported in Methods Sec. D.

a pure molecular state is prepared (i.e., the episode terminates) in one to two sweeping cycles. Episodes sometimes require more than one sweeping cycle to terminate since certain pulses (pulses 3, 4, 9, see grey parentheses in Table Extended 2) drive the population into multiple destinations. The average number of steps (9.7) needed is slightly lower than that

in one sweeping cycle (13 for $J \in \{1, 2\}$), indicating probable terminations of episodes due to projective measurements collapsing on states with relatively low populations.

Now, the same task of state preparation is assigned to the RL agent. The effectiveness of the protocol is straightforward to observe in Fig. 2b, as the average number of required pulse and measurement steps (or length) per preparation episode (blue) outperforms that achieved by the sweeping protocol (purple). Episodes with longer lengths are also observed, particularly early in the training, due to the intentionally suboptimal pulse choices. Such experiences, despite adverse, allow the RL agent to explore the pulse choices that are not locally optimal but may yield higher global reward in the long term (Methods Sec. D). One resulting protocol is presented as a decision tree in Fig. 2c (truncated, complete version in Fig. Extended 4). The cumulative probability of the successful pure-state preparation episodes (Fig. 2c, bottom) with the RL-designed protocol outperforms that from the referenced sweeping protocol when the same number of pulses is applied. The RL-designed protocol applies available pulses non-repetitively at the beginning, which resembles the sweeping protocol, while the repetitive application of one pulse is more common as the state preparation progresses. 71% of the episodes end on the $|J, -J + 1/2, -\rangle$ and $|J, -J - 1/2, -\rangle$ states (Fig. Extended 5), and a smaller fraction end on the states that belong to $\xi = '+'$ subspaces. We note that the reported decision tree is not unique among those that give similar cumulative success probability, as different decision trees can be obtained from independent trainings with stochastic initialization of the state-action value network. However, as shown in the pulse action histogram (bottom), smart utilization of the pulses that drive multiple transitions (pulses 3, 4, 9) is common in those decision trees and enhance the efficiency of state preparation.

Fig. 3 examines the performance of the RL-designed algorithm subject to environmental disturbance. Here, we consider the effect of black body radiation (BBR), one major source of experimental noise in molecular state control[19]. The strength of the thermal noise is quantified by BBR temperature, T_{BBR} , in Fig. 3a (see Methods Sec. C). The molecule is initialized in a Boltzmann distribution at 300 K independent of T_{BBR} . Regardless of the population distribution, BBR attempts to drive the system to thermal equilibrium and thus adversely affect the state preparation protocols (e.g. solid purple in Fig. 3a, $T_{\text{BBR}} = 400$ K v.s. 0 K). As shown in Fig. 3a, an environment with stronger thermal noise requires an increased

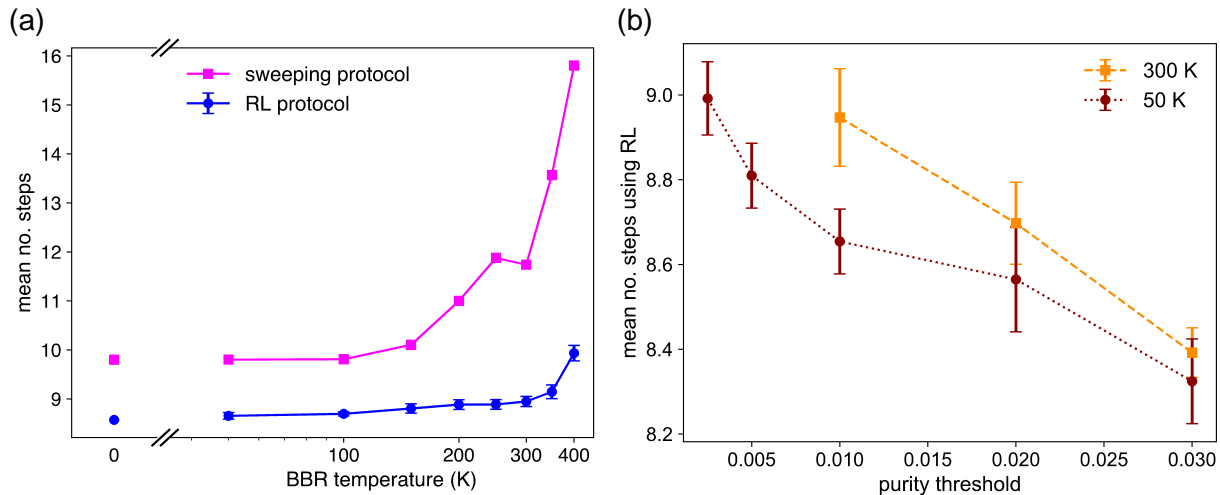


FIG. 3. **(a)** Mean number of steps to prepare a pure molecular state using the sweeping protocol and reinforcement learning algorithm at different BBR temperatures. The results are averaged over five independent training/testing sessions. The initial population of the states follows a Boltzmann distribution at 300K with the purity threshold set to 0.99, the same as those used in Fig. 2. The error bar denotes the standard deviation of the mean. **(b)** Mean number of steps to reach a pure state for different purity thresholds, at BBR temperatures of 50K and 300K. Simulations with purity thresholds of 0.0025 or 0.005 at 300K require more than 100 pulses to terminate due to thermally driven transitions.

number of pulses to prepare the single state, while the RL-designed protocol presents an obvious advantage (solid blue v.s. purple). Figure 3b presents the degree to which a single, pure state (purity, in the case of zero coherence) can be prepared with the RL approach under the BBR effects. The thermal noises limits the purity of the final molecular state (Fig. Extended 6), and an increased number of pulses are needed to complete the state preparation when the threshold decreases. Overall, our results demonstrate that the RL framework can be straightforwardly adapted to specific, realistic experimental settings.

Fig. 4 examines the applicability of the RL-designed protocol in systems with increasing dimensionality. For the aforementioned results involving molecular states from $J \in \{1, 2\}$ rotational manifold, the state-value function maps the population vector $S_t \in [0, 1]^{N_S=16}$ to the action optimality, $Q(S_t, a) \in \mathcal{R}^{N_A=13}$. However, for systems of up to $J \in \{1, 2, 3, 4\}$ ($[0, 1]^{48} \rightarrow \mathcal{R}^{68}$) and $J \in \{1, 2, 3, 4, 5, 6\}$ ($[0, 1]^{96} \rightarrow \mathcal{R}^{131}$) rotational manifolds, particularly

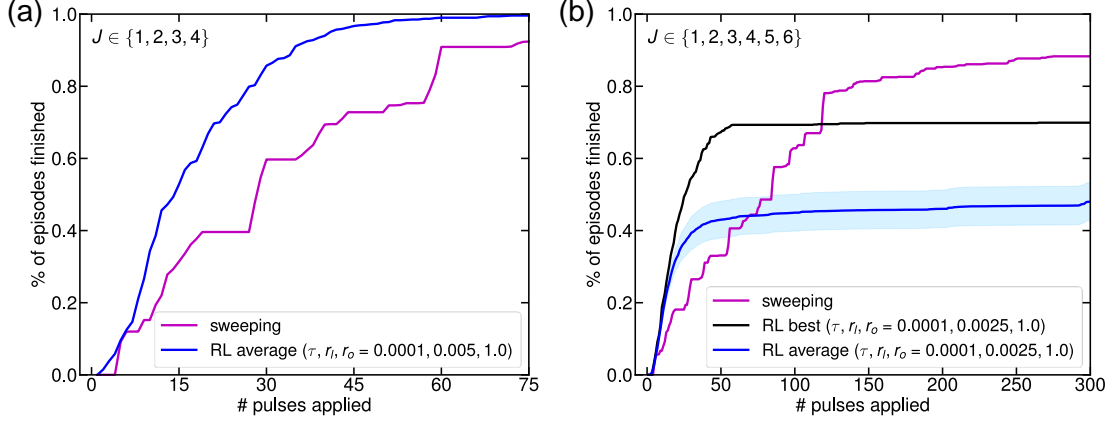


FIG. 4. **(a-b)** Percentage of finished episodes as a function of the number of the pulses applied, in the system that consists of rotational states from $J \in \{1, 2, 3, 4\}$ **(a)**, with 48 states and a library of 68 pulses to choose from), and $J \in \{1, 2, 3, 4, 5, 6\}$, **(b)**, with 96 states and a library of 131 pulses). Results are obtained with the sweeping protocol (solid purple) and the RL algorithm (solid blue). The blue curves are obtained by averaging over 5 (left) and 10 (right) independent training/testing sessions under the optimal hyperparameters, respectively. The shadow area indicates the standard deviation of the mean.

with a pulse library that includes as many possible same- J transitions with non-zero Rabi rates (see Methods [Sec. C](#), Figs. [Extended 7](#), [Extended 8](#), and [Extended 9](#)), the dimensionality poses a challenge to the learning process. In fact, the same procedure that works well for $J \in \{1, 2\}$ system leads to unsatisfactory learning performance when applied to such problems due to under-exploration. To address this challenge, we leverage our experience with the smaller system to perform physics-informed learning. Specifically, we set the reward function to additionally discourage the application of a pulse on the state S_t , if the resulting state and the previous one largely overlap each other, i.e. if $o(S_t, S_{t+1}) > 1 - 1/N_S$ with $o(S_t, S_{t+1}) := S_t \cdot S_{t+1} / (|S_t||S_{t+1}|)$. The extent to which the overlap shall be discouraged introduces another empirical tuning parameter, r_o , in the practical implementation. Fig. 4 compares the cumulative success ratio of the episodes from the RL-designed protocol to that from the referenced sweeping protocol (solid blue v.s. purple in Fig. 4a). It is clear that the RL curves have steeper slopes, indicating more successful termination when few pulses are applied. The RL success ratio also reaches unity more efficiently compared to the reference

protocol. The optimal value of r_o is usually near 1 or 2, suggesting that a balanced consideration of fast completion and low overlap results in the optimal performance of the training. Furthermore, when it comes to a problem with even larger dimensions, the improved performance of the RL-designed protocol is consistent ($J \in \{1, 2, 3, 4, 5, 6\}$ system, Fig. 4b, solid black v.s. purple), although both two cumulative success ratios reach unity at a slower pace. Quite interestingly, the RL agent designs an algorithm in which around 70% of the episodes quickly terminate, at the cost of very slow termination of the other episodes after about 40 pulses. In realistic settings, one could enforce a start-over once an upper limit of the number of pulses has been attempted for efficiency purposes. We recognize that a full exploration of the state-action transition pairs in such high-dimensional training remains a challenging task as the learning outcome highly depends on the initialized weight of the network (solid blue).

In summary, we have introduced reinforcement learning (RL) as a general, powerful, and flexible strategy to control the quantum states of the trapped molecular ion for the first time, to the best of our knowledge. Combined with the projective measurement approach realized with quantum logic spectroscopy (QLS), the RL approach leverages historical information of pulse choices and measurement outcomes to guide the selection of the next pulses to apply for pure state preparation. Notably, the RL approach works without the assumption of distinguishable transitions that the previous control protocol relies on, and this feature makes the approach particularly powerful when molecules with complex rovibrational structures, or molecules with a large number of thermally accessible states are of interest. It is worth mentioning that the decision tree results from this work (e.g. similar to that in Fig. 3b) could be directly implemented in experiments with minimal real-time computational cost.

The current study opens the door for a variety of future advancements at the intersection of physics and AI. Naturally, the utilization of other RL algorithms and neural network architecture that are particularly effective at exploring the immense state-action space might lead to improved performance and faster learning, as long as the computational runtime to execute the action selection procedure is shorter than the wall-clock duration of pulses in realistic experiments. In addition, not only can RL be applied to select the pulse sequences from a pre-determined library as in the current work, RL approaches can be directly employed to optimize the pulse shape in a continuous action space. From a physical perspective,

apart from designing the protocols that are resilient to experimental imperfection as we demonstrated, RL could offer a complementary tool to understand the experimental noises and uncertainties from a bottom-up perspective. In conclusion, we expect that the RL framework developed in this study will be of broad interest and practical usefulness at the intersection of AI-enabled precision control, quantum information science, and AMO physics.

ACKNOWLEDGEMENTS

The authors acknowledge Kristian D. Barajas, Dr. Muhammad M. Khan, Byoungwoo Kang, Dr. Tingrei Tan, Dr. Yu Liu and Dr. Hannah Knaack for helpful discussions of various aspects of this work. This research used resources of the National Energy Research Scientific Computing Center, a DOE Office of Science User Facility supported by the Office of Science of the U.S. Department of Energy under Contract No. DE-AC02-05CH11231. This work was supported by NSF CAREER Award under grant number ECCS 2246394, NSF QuSeC-TAQS 2326840 and NSF ExpandQISE 2231387. P.N. gratefully acknowledges support from the Gordon and Betty Moore Foundation grant No. GMBF 8048 and from the John Simon Guggenheim Memorial Foundation (Guggenheim Fellowship). D.R.L. acknowledges support from the Gordon and Betty Moore Foundation under grant No. GMBF 12252.

-
- [1] M. Safronova, D. Budker, D. DeMille, D. F. J. Kimball, A. Derevianko, and C. W. Clark, [Reviews of Modern Physics](#) **90**, 025008 (2018).
 - [2] D. DeMille, N. R. Hutzler, A. M. Rey, and T. Zelevinsky, [Nature Physics](#) **20**, 741 (2024).
 - [3] M. Kozlov and S. Levshakov, [The Astrophysical Journal](#) **726**, 65 (2010).
 - [4] V. Letokhov, [Physics Letters A](#) **53**, 275 (1975).
 - [5] M. Quack, G. Seyfang, and G. Wichmann, [Chemical Science](#) **13**, 10598 (2022).
 - [6] D. Mitra, K. H. Leung, and T. Zelevinsky, [Physical Review A](#) **105**, 040101 (2022).
 - [7] D. Patterson, [Physical Review A](#) **97**, 033403 (2018).
 - [8] E. R. Hudson, [EPJ Techniques and Instrumentation](#) **3**, 1 (2016).
 - [9] D. McCarron, M. Steinecker, Y. Zhu, and D. DeMille, [Phys. Rev. Lett.](#) **121**, 013202 (2018).

- [10] S. Ospelkaus, K.-K. Ni, G. Quéméner, B. Neyenhuis, D. Wang, M. H. G. de Miranda, J. L. Bohn, J. Ye, and D. S. Jin, *Phys. Rev. Lett.* **104**, 030402 (2010).
- [11] Y. Zeng, A. Jadbabaie, A. N. Patel, P. Yu, T. C. Steimle, and N. R. Hutzler, *Phys. Rev. A* **108**, 012813 (2023).
- [12] C. E. Dickerson, A. N. Alexandrova, P. Narang, and J. P. Philbin, arXiv preprint arXiv:2310.01534 (2023).
- [13] P. O. Schmidt, T. Rosenband, C. Langer, W. M. Itano, J. C. Bergquist, and D. J. Wineland, *Science* **309**, 749 (2005).
- [14] D. Leibfried, *New Journal of Physics* **14**, 023029 (2012).
- [15] S. Ding and D. Matsukevich, *New Journal of Physics* **14**, 023028 (2012).
- [16] C.-w. Chou, C. Kurz, D. B. Hume, P. N. Plessow, D. R. Leibbrandt, and D. Leibfried, *Nature* **545**, 203 (2017).
- [17] Y. Lin, D. R. Leibbrandt, D. Leibfried, and C.-w. Chou, *Nature* **581**, 273 (2020).
- [18] C.-w. Chou, A. L. Collopy, C. Kurz, Y. Lin, M. E. Harding, P. N. Plessow, T. Fortier, S. Didams, D. Leibfried, and D. R. Leibbrandt, *Science* **367**, 1458 (2020).
- [19] Y. Liu, J. Schmidt, Z. Liu, D. R. Leibbrandt, D. Leibfried, and C.-w. Chou, *Science* **385**, 790 (2024).
- [20] N. Schwegler, D. Holzzapfel, M. Stadler, A. Mitjans, I. Sergachev, J. Home, and D. Kienzler, *Phys. Rev. Lett.* **131**, 133003 (2023).
- [21] M. Sinhal, Z. Meir, K. Najafian, G. Hegi, and S. Willitsch, *Science* **367**, 1213 (2020).
- [22] P. Micke, T. Leopold, S. A. King, E. Benkler, L. J. Spieß, L. Schmöger, M. Schwarz, J. R. Crespo López-Urrutia, and P. O. Schmidt, *Nature* **578**, 60 (2020).
- [23] A. Landau, E. Eduardus, D. Behar, E. R. Wallach, L. F. Pašteka, S. Faraji, A. Borschevsky, and Y. Shagam, *The Journal of Chemical Physics* **159** (2023).
- [24] X.-M. Zhang, Z. Wei, R. Asad, X.-C. Yang, and X. Wang, *npj Quantum Information* **5**, 85 (2019).
- [25] Z. An, H.-J. Song, Q.-K. He, and D. Zhou, *Physical Review A* **103**, 012404 (2021).
- [26] J. Mackeprang, D. B. R. Dasari, and J. Wrachtrup, *Quantum Machine Intelligence* **2**, 1 (2020).
- [27] I. Paparella, L. Moro, and E. Prati, *Physics Letters A* **384**, 126266 (2020).
- [28] M. Y. Niu, S. Boixo, V. N. Smelyanskiy, and H. Neven, *npj Quantum Information* **5**, 33 (2019).

- [29] F. Preti, M. Schilling, S. Jerbi, L. M. Trenkwalder, H. P. Nautrup, F. Motzoi, and H. J. Briegel, *Quantum* **8**, 1343 (2024).
- [30] R. S. Sutton and A. G. Barto, *Reinforcement learning: An introduction* (MIT press, 2018).
- [31] V. Mnih, K. Kavukcuoglu, D. Silver, A. Graves, I. Antonoglou, D. Wierstra, and M. Riedmiller, arXiv preprint arXiv:1312.5602 (2013).
- [32] V. Mnih, K. Kavukcuoglu, D. Silver, A. A. Rusu, J. Veness, M. G. Bellemare, A. Graves, M. Riedmiller, A. K. Fidjeland, G. Ostrovski, *et al.*, *Nature* **518**, 529 (2015).
- [33] C. J. Watkins, *Learning from delayed rewards*, Ph.D. thesis, King’s College, Cambridge United Kingdom (1989).
- [34] A. Paszke, S. Gross, F. Massa, A. Lerer, J. Bradbury, G. Chanan, T. Killeen, Z. Lin, N. Gimeshain, L. Antiga, *et al.*, *Advances in neural information processing systems* **32** (2019).
- [35] J. R. Johansson, P. D. Nation, and F. Nori, *Computer physics communications* **183**, 1760 (2012).
- [36] J. Johansson, P. Nation, and F. Nori, *Computer Physics Communications* **184**, 1234 (2013).
- [37] J. Schulman, F. Wolski, P. Dhariwal, A. Radford, and O. Klimov, arXiv preprint arXiv:1707.06347 [10.48550/arXiv.1707.06347](https://arxiv.org/abs/10.48550/arXiv.1707.06347) (2017).
- [38] A. L. Collopy, J. Schmidt, D. Leibfried, D. R. Leibbrandt, and C.-W. Chou, *Physical Review Letters* **130**, 223201 (2023).
- [39] C. H. Townes and A. L. Schawlow, *Microwave spectroscopy* (McGRAW-HILL BOOK COMPANY, 1955).
- [40] A. Corney, *Atomic and laser spectroscopy* (Clarendon Press, 1977).
- [41] P. Virtanen, R. Gommers, T. E. Oliphant, M. Haberland, T. Reddy, D. Cournapeau, E. Burovski, P. Peterson, W. Weckesser, J. Bright, S. J. van der Walt, M. Brett, J. Wilson, K. J. Millman, N. Mayorov, A. R. J. Nelson, E. Jones, R. Kern, E. Larson, C. J. Carey, Í. Polat, Y. Feng, E. W. Moore, J. VanderPlas, D. Laxalde, J. Perktold, R. Cimrman, I. Henriksen, E. A. Quintero, C. R. Harris, A. M. Archibald, A. H. Ribeiro, F. Pedregosa, P. van Mulbregt, and SciPy 1.0 Contributors, *Nature Methods* **17**, 261 (2020).
- [42] J. Huerta-Cepas, F. Serra, and P. Bork, *Molecular biology and evolution* **33**, 1635 (2016).

METHODS

A. State evolution in the preparation process

We consider a molecular spectroscopy ion that occupies ground electronic and vibrational states, while a substantial number of its rotational states are accessible due to blackbody radiation. The resulting density matrix of the rotational manifold is $\rho = \sum_{\mathcal{J}=1}^{N_S} P_{\mathcal{J}} |\mathcal{J}\rangle \langle \mathcal{J}|$, with N_S the number of states, and $P_{\mathcal{J}} = e^{-\beta E_{\mathcal{J}}} / \sum_{\mathcal{J}} e^{-\beta E_{\mathcal{J}}}$ following a Boltzmann distribution. The co-trapped logic Ca^+ ion is prepared in a $|D\rangle$ state and a motional mode $|k\rangle$ is shared between the spectroscopic ion and the logic ion. In this section, we present the equations for the case where one excited motional state is accessible (Lamb-Dicke regime) for illustration purposes, approximating that the projective measurement gives identical positive signals for $k = 1$ and higher excited motional states $k > 1$ (more precisely, the blue motional sideband pulse on the logic ion drives the populations of different motional states with different Rabi frequencies). The applied laser pulse drives the molecular transition and results in a quantum state with a density matrix of

$$\rho = \sum_{\mathcal{J}=1}^N P_{\mathcal{J}} \left[\left(\sum_{\mathcal{J}'} u_{\mathcal{J}\mathcal{J}'} |\mathcal{J}', 0\rangle + \sum_{\mathcal{J}'} v_{\mathcal{J}\mathcal{J}'} |\mathcal{J}', 1\rangle \right) \left(\sum_{\mathcal{J}'} u_{\mathcal{J}\mathcal{J}'}^* \langle \mathcal{J}', 0| + \sum_{\mathcal{J}'} v_{\mathcal{J}\mathcal{J}'}^* \langle \mathcal{J}', 1| \right) \right]. \quad (\text{S1})$$

In Eq. S1, the molecular ion has a probability of $P_{\mathcal{J}}$ to occupy the state $|\mathcal{J}\rangle$ and interacts with the laser pulse, and $u_{\mathcal{J}\mathcal{J}'}$ and $v_{\mathcal{J}\mathcal{J}'}$ describes the time evolution of a pure state $|\mathcal{J}, 0\rangle$ under the influence of the applied pulse. Subsequently, a motional sideband pulse is applied on the logic ion in order to map the motional state onto the Ca^+ ion internal state, and a projective measurement of the motional state can now be performed with a fluorescence observation on the quantum state of the logic ion (i.e. to identify whether the Ca^+ ion is in state $|D\rangle$ or $|S\rangle$). The projective measurement collapses the quantum state probabilistically according to the outcome. After the measurement and the subsequent motional state cooling, the state of the molecular spectroscopy ion is

$$\rho = \begin{cases} (1/p_1) \sum_{\mathcal{J}'} (\sum_{\mathcal{J}} P_{\mathcal{J}} |v_{\mathcal{J}\mathcal{J}'}|^2) |\mathcal{J}'\rangle \langle \mathcal{J}'|, & \text{if } k = 1, p_1 = \sum_{\mathcal{J}, \mathcal{J}'} P_{\mathcal{J}} |v_{\mathcal{J}\mathcal{J}'}|^2 \\ (1/p_0) \sum_{\mathcal{J}'} (\sum_{\mathcal{J}} P_{\mathcal{J}} |u_{\mathcal{J}\mathcal{J}'}|^2) |\mathcal{J}'\rangle \langle \mathcal{J}'|, & \text{if } k = 0, p_0 = \sum_{\mathcal{J}, \mathcal{J}'} P_{\mathcal{J}} |u_{\mathcal{J}\mathcal{J}'}|^2 \end{cases}, \quad (\text{S2})$$

with k denoting the measured outcome of the motional state, and p_k is the probability of the outcome k . Laser pulse applications and projective measurements is then repeated many times until a pure state has been prepared. Note that we consider a molecular state pure with a small tolerance of η .

B. Time evolution with the adiabatically-eliminated Hamiltonian

Accurate construction of the transition matrices (TMs, i.e. \mathcal{A} s) in the Markov decision process is the key so that the model faithfully reflects the physical process. Those TMs describe the effects of the pulse operations on the molecular quantum state and allow for a compact description of the system’s time evolution. Since motional state cooling is performed after every pulse/measurement in the current state preparation scheme, we assume that coherence is destroyed by the cooling, and thus only the population vectors are tracked during the time evolution (Fig. 1c). This way, the description of population dynamics is condensed to a compact set of $2N_A$ TMs (with the size of $N_S \times N_S$) for input into the RL calculations.

We evaluate the TMs by numerically solving the time-dependent Schrödinger Equation with the realistic pulse characteristics (frequencies, amplitudes, and durations). The total Hamiltonian of the system (in the laboratory frame) consists of two components, the time-independent molecular hyperfine Hamiltonian (Eq. S5) and the time-dependent pulse-molecule interactions,

$$H_{\text{int}} = \sum_{\mathcal{J} < \mathcal{J}'} \frac{\Omega_{\mathcal{J}, \mathcal{J}'}}{2} \left[e^{i[\lambda_{\text{LD}}(a_{\text{mot}} + a_{\text{mot}}^\dagger) - \omega t]} |\mathcal{J}'\rangle \langle \mathcal{J}| + h.c. \right] \quad (\text{S3})$$

where $\Omega_{\mathcal{J}, \mathcal{J}'}$ is the Rabi frequency between states $|\mathcal{J}\rangle$ and $|\mathcal{J}'\rangle$ and is obtained by adiabatically eliminating the intermediate states[16] (see Eq. S6). λ_{LD} is Lamb-Dicke parameter, a_{mot} and a_{mot}^\dagger are the annihilation and creation operators for the motional mode, and ω is the laser frequency. For numerical stability, only the first-order terms in the Lamb-Dicke parameter are kept in the simulations, i.e. we assume that $\exp[i \lambda_{\text{LD}}(a + a^\dagger)] = \mathbb{I} + i \lambda_{\text{LD}}(a_{\text{mot}} + a_{\text{mot}}^\dagger)$ for $\lambda_{\text{LD}} = 0.09$. The numerical calculations are performed with the QuTiP software package[35, 36]. As plotted in Fig. Extended 1, a comparison of the Rabi oscillations between the simulation and the experiment observations[16] demonstrates the effectiveness of the simulation protocol.

We also consider the effects of black body radiation (BBR), a major source of experimental noise. Competing with the aforementioned efforts to concentrate the population to a specific state, BBR steers the state populations back to their thermal equilibrium. Time evolution of the probability distribution of each state follows the coupled rate equations under the influence of BBR,

$$\frac{dP_{\mathcal{J}}(t)}{dt} = - \sum_{\mathcal{J}' \neq \mathcal{J}} \mathcal{R}_{\mathcal{J} \rightarrow \mathcal{J}'} P_{\mathcal{J}} + \sum_{\mathcal{J}' \neq \mathcal{J}} \mathcal{R}_{\mathcal{J}' \rightarrow \mathcal{J}} P_{\mathcal{J}'}, \quad (\text{S4})$$

where $P_{\mathcal{J}}$ is the statistical population of occupying state $|\mathcal{J}\rangle$, $\mathcal{R}_{\mathcal{J} \rightarrow \mathcal{J}'}$ is the rate at which population from state \mathcal{J} transfers to state \mathcal{J}' . The rates are calculated using Einstein's A and B coefficients[19] for spontaneous and stimulated transitions (Eq. S7). In the simulations, we discretize the time into small intervals and approximate the BBR influence as a first-order expansion with respect to the discretized timestep to propagate Eq. S4.

C. Computational details: sweeping protocol, Hamiltonian, pulses

Sweeping protocol—We note that the sweeping protocol presented in the article differs slightly from the experimental protocol introduced by NIST. Specifically, in NIST experiments, a number of pulses are applied between the projective measurements[16, 19], while in our modeling, one projective measurement follows one applied pulse in every preparation step. We choose to perform measurements between the pulses to receive feedback on the instantaneous populations. Nevertheless, we use the sweeping protocol as a reference to report the reinforcement learning results and keep the name ‘sweeping protocol’ to credit the original authors for the development of the idea.

Molecular Hamiltonian—The time-independent molecular Hamiltonian for CaH^+ , under the influence of an external magnetic field, is[16]

$$H_{\text{mol}} = \frac{1}{\hbar}(2\pi R \hat{\mathbf{J}}^2 - g\mu_N \hat{\mathbf{J}} \cdot \mathbf{B} - g_I \mu_N \hat{\mathbf{I}} \cdot \mathbf{B} - 2\pi c_{IJ} \hat{\mathbf{I}} \cdot \hat{\mathbf{J}}), \quad (\text{S5})$$

where $\hat{\mathbf{J}}$ is the rotational angular momentum of the molecule, $\hat{\mathbf{I}}$ is the nuclear spin operator, \mathbf{B} is the magnetic field. R is the rotational constant, μ_N is the nuclear magneton, g and g_I are the rotational and nuclear g -factors, respectively, and c_{IJ} is the spin-rotation constant. The eigenstates are denoted as $|J, m, \xi\rangle$, where J is the total rotational quantum number,

m is the total magnetic quantum number and ξ indicates the relative sign in the eigenstate coefficients.

Raman Rabi rates—For a given set of two pump/Stokes pulses (with known amplitudes, polarization, frequencies, and duration), the Raman-Rabi frequency is given by

$$\Omega_{if} = \frac{1}{4\hbar^2} \sum_M \left(\frac{\langle f | \mathbf{d} \cdot \mathbf{E}_2 | M \rangle \langle M | \mathbf{d} \cdot \mathbf{E}_1 | i \rangle}{\omega_{iM} - \omega_1} + \frac{\langle f | \mathbf{d} \cdot \mathbf{E}_1 | M \rangle \langle M | \mathbf{d} \cdot \mathbf{E}_2 | i \rangle}{\omega_{iM} + \omega_2} \right) \quad (\text{S6})$$

where $\mathbf{E}_1, \mathbf{E}_2$ are the two driving fields with respective frequencies ω_1, ω_2 , \mathbf{d} is the permanent dipole, $\omega_{iM} = (E_M - E_i)/\hbar$ is the frequency difference of the initial, $|i\rangle$, and intermediate $|M\rangle$, states. The absorption pulse produces a π -polarized field and the stimulated emission pulse produces a σ^+/σ^- -polarized field. More details on the above expression can be found in [16, 38], and pg. 22-23 of [39]. It is worth mentioning that we do not apply the rotating wave approximation in Eq. S6, because two-photon Raman transitions can utilize a pump/Stokes laser that is far detuned from the intermediate states (i.e. $|\omega_{iM} - \omega_1|$ is comparable to $|\omega_{iM} + \omega_2|$). Faster Raman-Rabi rates indicate that the population transition takes less time to drive. The amplitudes of the laser pulses are set the same as in the experiment [16] such that the Rabi rate for transition $|1, -3/2, -\rangle \rightarrow |1, -1/2, -\rangle$ is $2.087 \times 2\pi$ kHz.

Black Body Radiation—The BBR rates are evaluated as

$$R_{i \rightarrow f} = \rho_{i,f}^{\text{BBR}}(\omega) B_{i,f} + A_{i,f} \quad (\text{S7})$$

where $R_{i \rightarrow f}$ is the transition probability from state i to state f , $A_{i,f}$ is stimulated emission probability, $B_{i,f}$ is the Einstein coefficient for stimulated emission and $\rho_{i,f}^{\text{BBR}}(\omega)$ is the energy density of black body radiation per unit bandwidth at angular frequency ω . Details on calculating these coefficients can be found in Chapter 9 of Ref. 40.

Considering a mixed state that is under the influence of BBR, after a small time step δt , the initial probability distribution $\mathbf{P} = \{P_1, P_2, \dots, P_{N_S}\}$ evolves into

$$\mathbf{P}(t + \delta t) = T\mathbf{P}(t), \quad (\text{S8})$$

where

$$T = I + \begin{bmatrix} -\sum_{k=1}^N \mathcal{R}_{1 \rightarrow k} & \mathcal{R}_{2 \rightarrow 1} & \dots & \mathcal{R}_{N \rightarrow 1} \\ \mathcal{R}_{1 \rightarrow 2} & -\sum_{k=1}^N \mathcal{R}_{2 \rightarrow k} & \dots & \mathcal{R}_{N \rightarrow 2} \\ \vdots & \vdots & \ddots & \vdots \\ \mathcal{R}_{1 \rightarrow N} & \mathcal{R}_{2 \rightarrow N} & \dots & -\sum_{k=1}^N \mathcal{R}_{N \rightarrow k} \end{bmatrix} \delta t$$

under a first-order expansion to δt . Therefore, for a duration of Δt , the BBR evolves the state population as

$$\mathbf{P}(t + \Delta t) = T^{\Delta t/\delta t} \mathbf{P}(t). \quad (\text{S9})$$

We propagate the system dynamics under the influence of pulse sequences and BBR effects in sequential order, which is a good approximation to the actual dynamics because the laser pulses are much shorter than the time constant for BBR-driven transitions.

Pulses that drive multiple transitions in $J = 1, 2$ —In Fig. 2, pulses 3, 4, 9 are shown to drive multiple transitions in different J -manifolds. The pulse frequencies and duration are chosen as the average of the two transition frequencies and π -pulse durations, respectively, except for pulse 3. We notice that the Rabi frequency for one of the transitions is almost three times faster than the other, thus the pulse duration is set to the π -pulse duration of the slower transition.

Computational Details: resolving the evolution transition matrices—We perform the simulation of state evolution with QuTip[35, 36] 4.7. We simulate the time-dependent Schrödinger Equation with *qutip.mesolve* and *qutip.propagator* functions with the aforementioned Hamiltonians (combining Eq. S5 and Eq. S3 together). We use the *zvode* ODE integrator as implemented in the SciPy library[41] and a timestep of $\sim 1 \mu\text{s}$ is used. Despite the state dynamics being described in terms of population vectors (as in Fig. 1c), we keep the coherence in the evolution of the quantum state, and only make this approximation, i.e. take the diagonal term in the end to resolve the transition matrices \mathcal{A} s. The time evolution of the statistical mixture with the total Hamiltonian, H_{tot} , is obtained by separately simulating the time evolution of each eigenstate of the H_{mol} , i.e. for $\rho(0) = \sum_{\mathcal{J}} P_{\mathcal{J}} |\mathcal{J}\rangle \langle \mathcal{J}|$,

$$\rho(t) = e^{-iH_{\text{tot}}t} \rho(0) e^{+iH_{\text{tot}}t} = \sum_{\mathcal{J}} P_{\mathcal{J}} |\mathcal{J}'(t)\rangle \langle \mathcal{J}'(t)|, \quad (\text{S10})$$

with $|\mathcal{J}'(t)\rangle = e^{-iH_{\text{tot}}t} |\mathcal{J}\rangle$.

Weak pulses—It is recognized that transitions with weaker Rabi rates (for a given amplitude of Raman pulses) are harder to drive in the experiments. In addition, Fig. Extended 10 presents the difficulty in the numerical procedure to simulate the time evolution for weak pulses. Numerical difficulties decrease if the pulses are intended to drive the stronger transition, quantified by larger Rabi rates (e.g. the results for 1', 2', 3', 4' under column 'mot2'). We note that the numerical difficulties can be ameliorated by including more motional states

in the simulations when using QuTip software. In this work, we construct the pulse library with pulses with minimum Rabi rates of $0.2 \times 2\pi$ kHz.

D. Computational details: Reinforcement learning agents

RL agents—We prefer the use of the off-policy Q -learning algorithm for the state preparation task because off-policy exploration can lead to better sample efficiency in the discrete action space. Nevertheless, we also examined the performance of another widely recognized RL algorithm, proximal policy optimization (PPO)[37]. It turns out that for $J \in \{1, 2\}$ systems, the PPO agent has a profoundly smaller success ratio of episode termination compared to the DQN agent, for tested batch size and learning rate hyperparameters across 3 magnitudes.

Q -learning algorithm—The Q -learning works by finding the current action a that maximizes the estimated expected cumulative reward

$$a = \arg \max_a Q(s, a) \quad (\text{S11})$$

with the state-action value function

$$Q(s, a) = \mathbb{E} \left[\sum_{\tau=0}^T R_{t+1+\tau} | S_t = s, A_t = a \right], \quad (\text{S12})$$

and T is the terminal step when the state with a purity of 1 (with a small tolerance of η) is prepared. $Q(s, a)$ are updated as a temporal difference learning through the process of the agent interacting with the environment. In this work, we focus on the deep Q -learning algorithm[31–33] with a simple, fully-connected network, and the RL training and testing are performed with PyTorch software[34].

Computational Details: training the RL agents—We implement the reinforcement learning agents to propose future actions according to the agent-environment interaction in the Markov decision process (Fig. 1). In this work, the generalized policy iteration of the task is completed with the model-free, temporal difference learning agent—the deep Q -learning (DQN) agent[31, 32]. We use experience replay and double- Q networks for robust and efficient training. We perform the hyperparameter tuning for the neural network update rate (τ) and the learning rate (r_l) by the analysis of state-action trajectories and the resulting decision tree obtained with training under different hyperparameters. The soft action selection

is implemented with the ε -greedy algorithm and the exploration parameter,

$$\varepsilon = \varepsilon_{\text{end}} + (\varepsilon_{\text{end}} - \varepsilon_{\text{start}}) \exp(-n_{\text{training}}/\tau_\varepsilon) \tag{S13}$$

decreases with the progress of the training. In Eq. S13, we choose a $\varepsilon_{\text{start}} = 1$, $\varepsilon_{\text{end}} = 0.005$, and $\tau_\varepsilon = 0.3N_{\text{training}}$ with n_{training} and N_{training} the current and the total number of training episodes, respectively.

Hyperparameter tuning for $J = 1, 2$ system—Since the agent-environment interaction in the example system is relatively simple, we find that training with a range of hyperparameters ($\tau = 0.0005, 0.001, 0.0025$, $r_l = 0.0005, 0.001$) can all lead to a RL agent with good performance (average number of episodes between 8.6 and 9.2). We report in Fig. 3 the reinforcement learning results obtained with $\tau = 0.0025$, $r_l = 0.0005$.

Hyperparameter tuning for $J = 1, 2$ system with BBR—We scanned a broader range of hyperparameters compared to the $J = 1, 2$ clean system ($\tau = 0.00025, 0.0005, 0.001, 0.0025, 0.005$; $r_l = 0.00025, 0.0005, 0.001, 0.0025, 0.005$) to ensure the RL agent’s performance for this noisy system. The RL algorithm underwent five independent training and testing sessions for each set of hyperparameters. The mean of each model was calculated from the last 500 episodes from the testing session. For each BBR temperature, the lowest mean from one set of hyperparameters was plotted in Fig. 4. The optimal hyperparameters for each BBR temperature are listed in Table. Extended 1.

BBR Temp. (K)	τ	r_l	BBR Temp. (K)	τ	r_l
0	0.005	0.0005	50	0.0005	0.0005
100	0.0005	0.0005	150	0.0005	0.001
200	0.001	0.0005	250	0.0025	0.0005
300	0.0005	0.0005	350	0.001	0.0005
400	0.0005	0.0005			

TABLE Extended 1. Optimal hyperparameters for each BBR temperature.

Hyperparameter tuning for $J \leq 4$ and $J \leq 6$ system—Hyperparameter scans are performed for τ , r_l , and r_o independently (scan over two magnitudes for τ and r_l , and one magnitude for r_o) and the optimal combination of parameters have been reported in Fig. 4. We also tested the use of a neural network with four fully connected layers in the

RL calculations for $J \leq 6$ system (with the same, and longer training episodes). The state preparation episodes finish with longer durations.

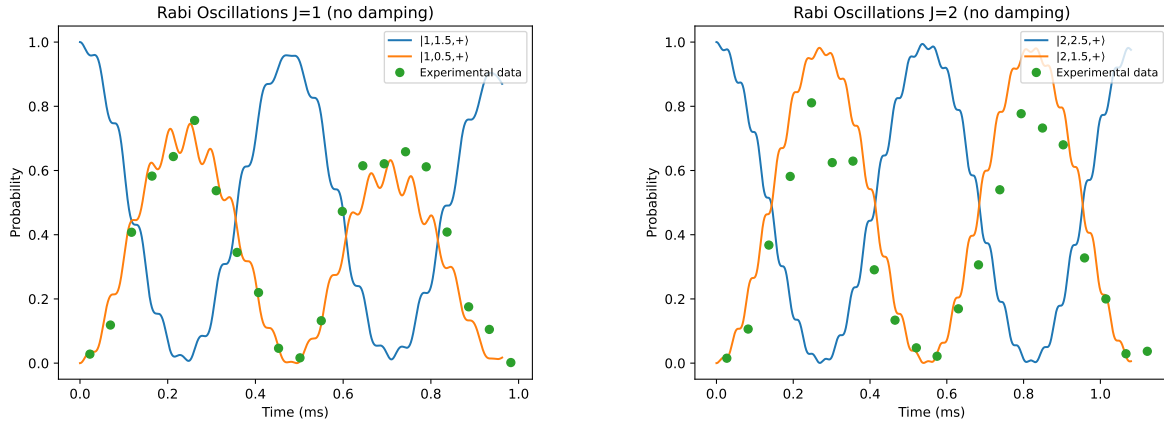
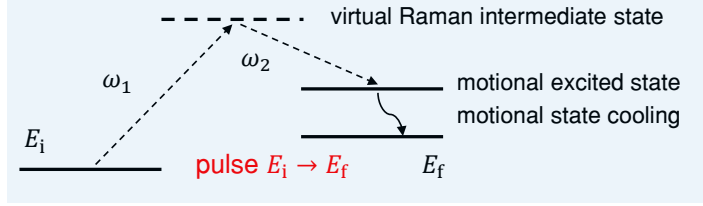


FIG. Extended 1. Rabi oscillations between states $|J, -J-1/2, -\rangle \leftrightarrow |J, -J+1/2, -\rangle$ for the $J = 1, 2$ manifolds are simulated without noise, and compared to experimental data[16]. In [Extended 1](#), the plots are obtained by dynamically evolving the system using the *mesolve* function in QuTip. The the initial state vector is set to have a concentrated population on state $|J, -J + 1/2, +\rangle$.



Pulse	$f = \Delta E/h - \nu_m$ (kHz)	Ω (2π kHz)	D (ms)
1	-1.72	2.156	16.2
2	-1.44	1.008	34.6
3	-1.03 (-1.01, -1.06)	0.621, 2.138	52.6
4	-0.23 (-0.17, -0.30)	1.881, 1.857	18.7
5	4.40	1.223	28.5
6	26.13	1.174	29.7
7	-6.12	2.097	16.6
8	-6.56	0.621	56.2
9	-7.33 (-7.40, -7.26)	1.221, 1.857	23.7
10	9.87	2.078	16.8
11	-9.87	2.078	16.8
12	13.13	1.852	18.8
13	-13.13	1.852	18.8

TABLE Extended 2. Optical pumping transitions in Fig. 2a consist of a two-photon stimulated Raman process, followed by motional state cooling. Pulse sequence parameters, including transition frequencies f (transition energies $\Delta E = E_f - E_i$, reported as difference from the motional mode frequency, $\nu_{\text{mot}} = 5.164$ MHz), Rabi rates Ω , and the pulse duration D . The duration is chosen such that the pulses are close to π -pulses, i.e. $D = \pi/(\lambda_{\text{L-D}}\Omega)$ with $\lambda_{\text{L-D}}$ the Lamb-Dicke parameter.

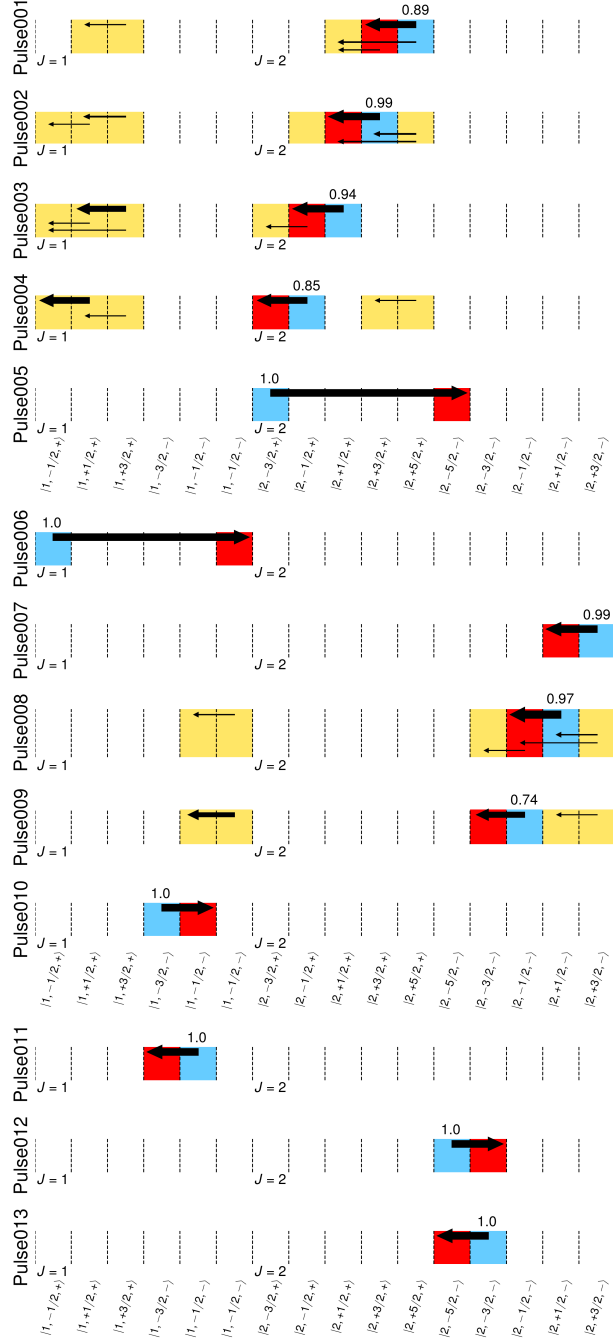


FIG. Extended 2. State population transfer driven by the 13 pulses described in Fig. 2 for $J = 1, 2$ rotational manifold. The main transition is color-coded as arrows from blue to red boxes, and the amount of the population transition is listed above the arrow. The width of the arrows indicates the amount of the population transition and for each pulse, the most significant five transitions are plotted. By driving the blue-sideband transitions and controlling the pulse polarization, those pulses drive the population transfer in one direction.

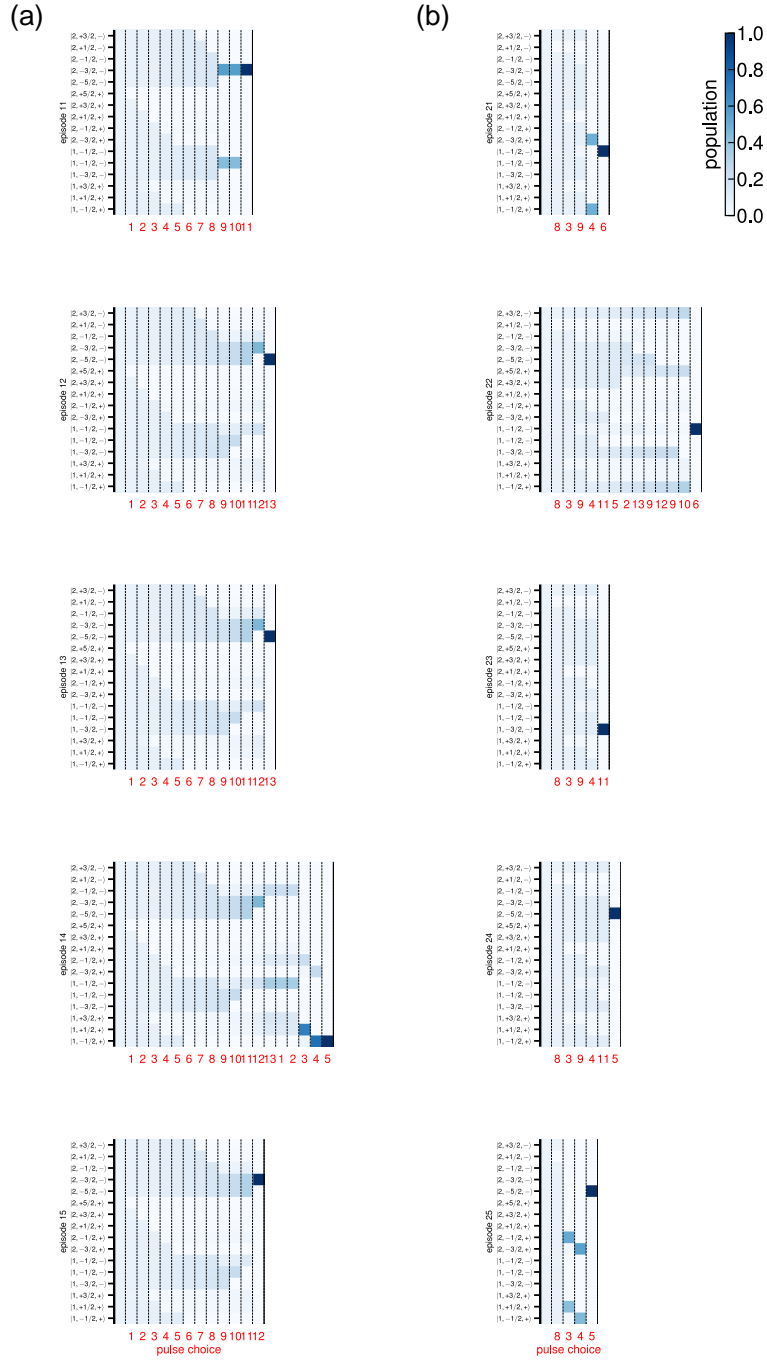


FIG. Extended 3. Dynamics of state populations, $P(\mathcal{J}) = \text{tr}(\rho|\mathcal{J}\rangle\langle\mathcal{J}|)$, from typical state-action trajectories in the Markov decision processes with (a) sweeping and (b) the RL-designed protocol.

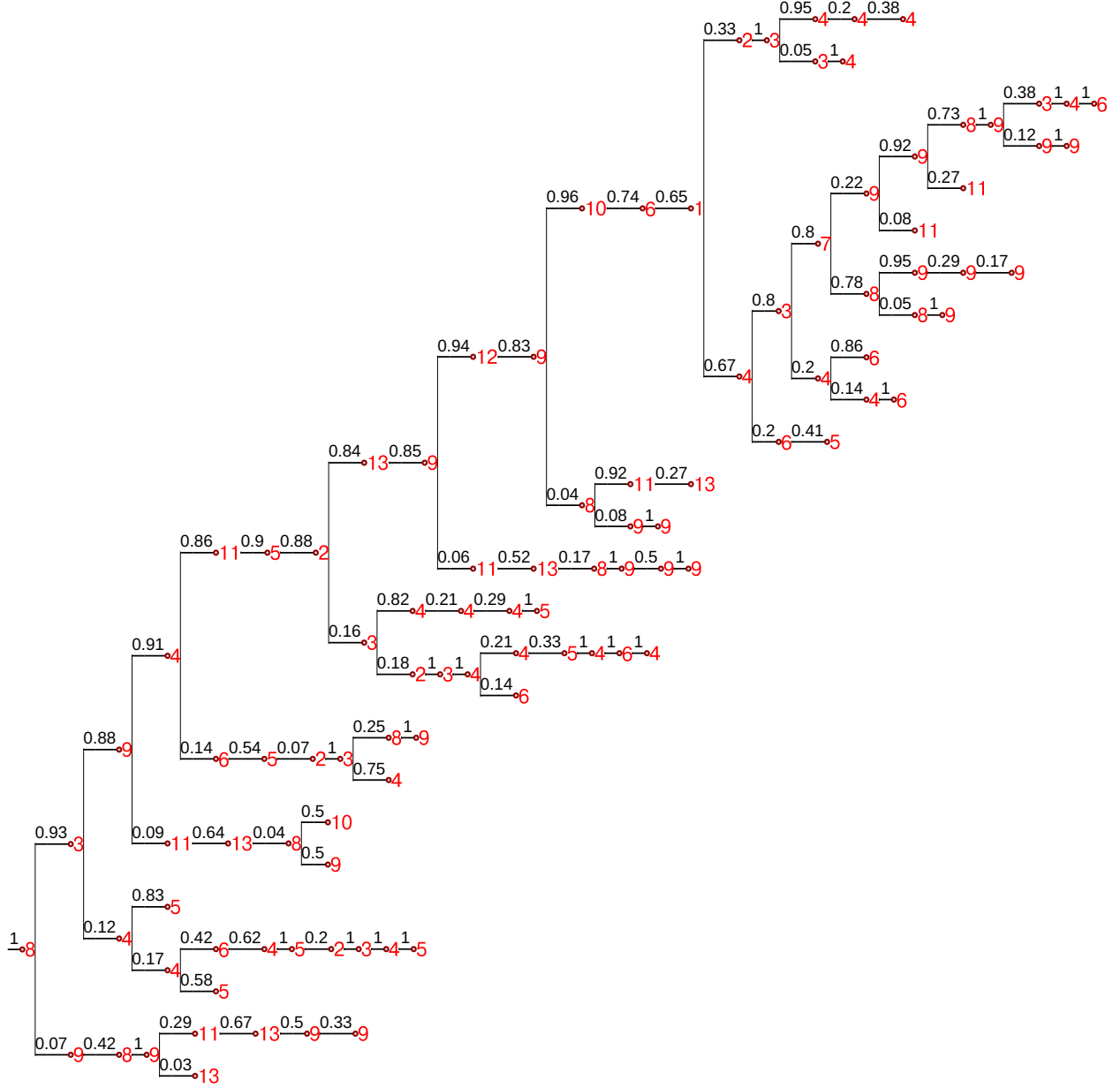


FIG. Extended 4. A complete version of the decision tree plotted in the main Fig. 3. The pulse choices are reported in red, and the branching probabilities are reported in black. Most of the time the parent node has two offspring nodes, corresponding to the two, $k = 0$ and $k = 1$, measurement results, respectively. However, we also observe nodes with more than two offspring because sometimes the optimal pulse choices are coincidentally the same for two different quantum states. The branch that leads to episode termination (blue boxes in Fig. 2) is omitted in the plot. The tree plot is produced with the ETE library[42].

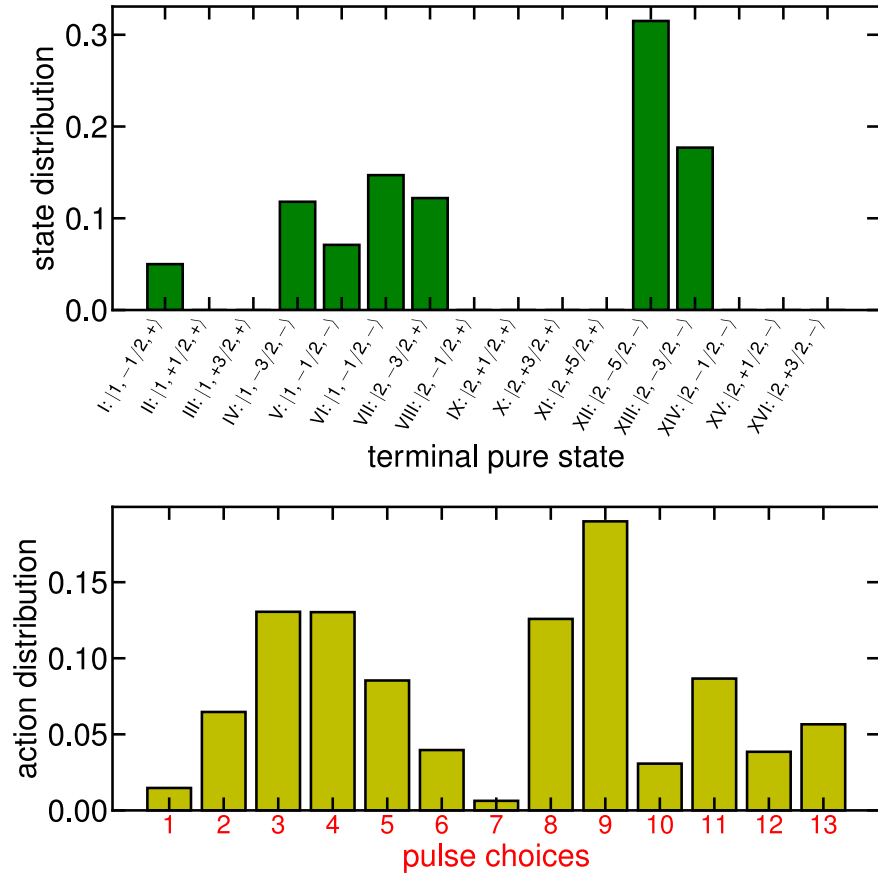


FIG. Extended 5. Statistical distribution of the termination single states (top), and of the pulse sequence choices (bottom) in the testing episodes.

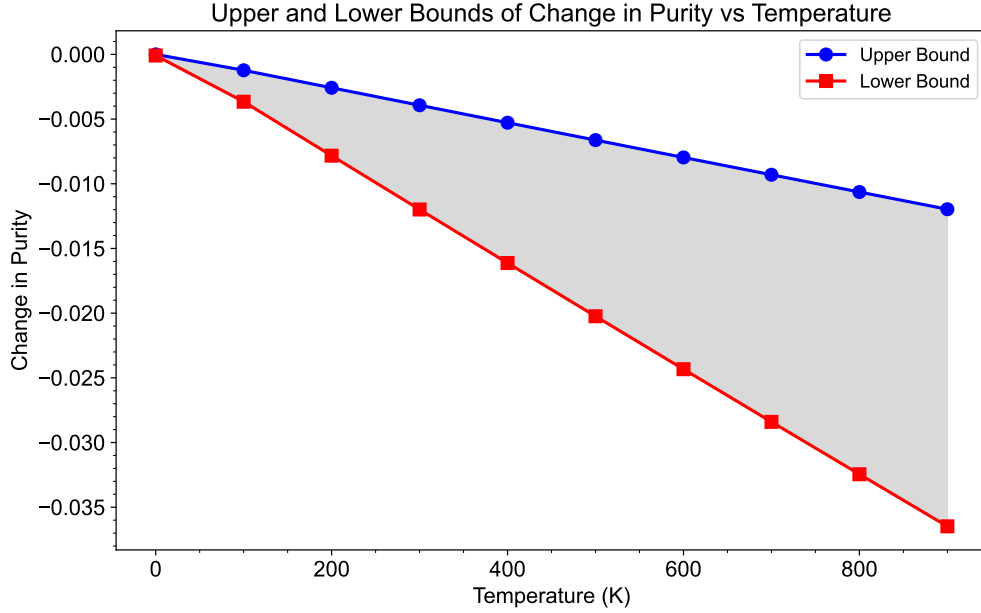


FIG. Extended 6. Lower and upper bounds of the degradation in purity due to thermal excitations during a single pulse/measurement step in the state space of manifolds $J = 1, 2$. The lower bound is calculated by evolving each pure rotational state under blackbody radiation (BBR) for the duration of the longest laser pulse in the pulse library. Each state’s purity degrades differently based on the coupling strengths of BBR-driven transitions. The maximum purity degradation defines the lower bound, while the upper bound is similarly obtained using the shortest pulse duration. This analysis shows that BBR is responsible when the reinforcement learning (RL) protocol is near termination but fails due to thermal excitations.

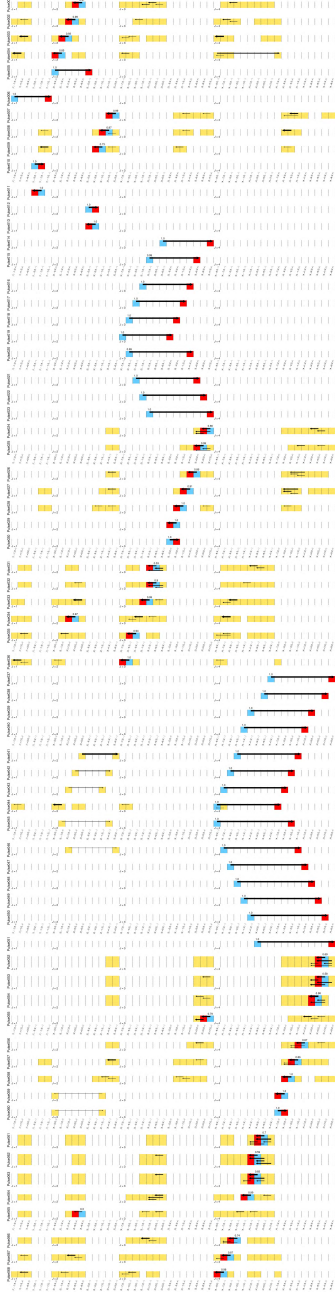


FIG. Extended 7. Pulse library for $J \in \{1, 2, 3, 4\}$ system learning in Fig. 4. The results are obtained with a simulation that includes 4 motional states. The main transition is color-coded as arrows from blue to red boxes, and the amount of the population transition is listed above the arrow. The width of the arrows indicates the amount of the population transition and for each pulse, the most significant five transitions are plotted.

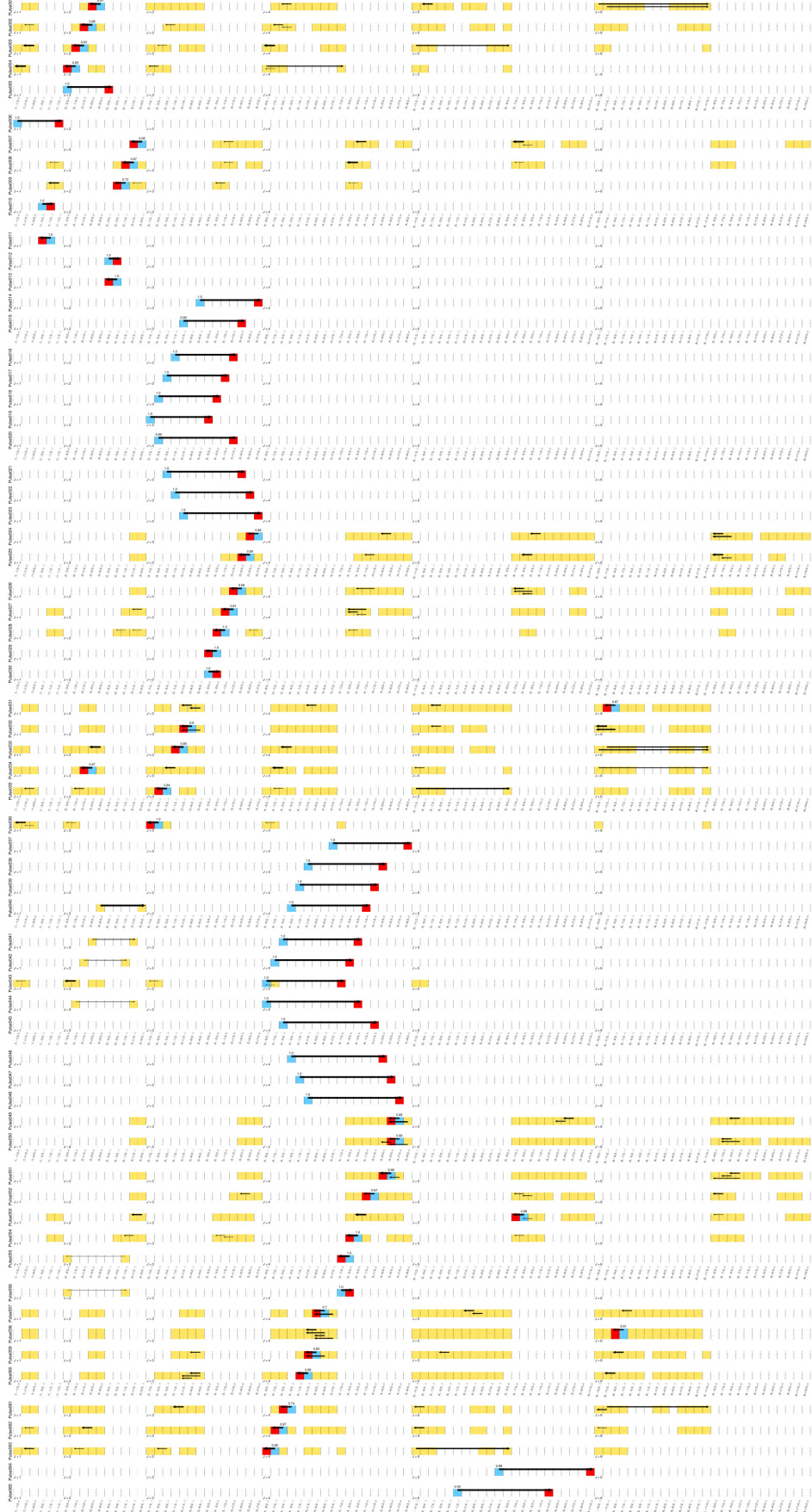


FIG. Extended 8. Pulse library for $J \in \{1, 2, 3, 4, 5, 6\}$ system learning in Fig. 4 (part 1). The results are obtained with a simulation that includes 4 motional states.

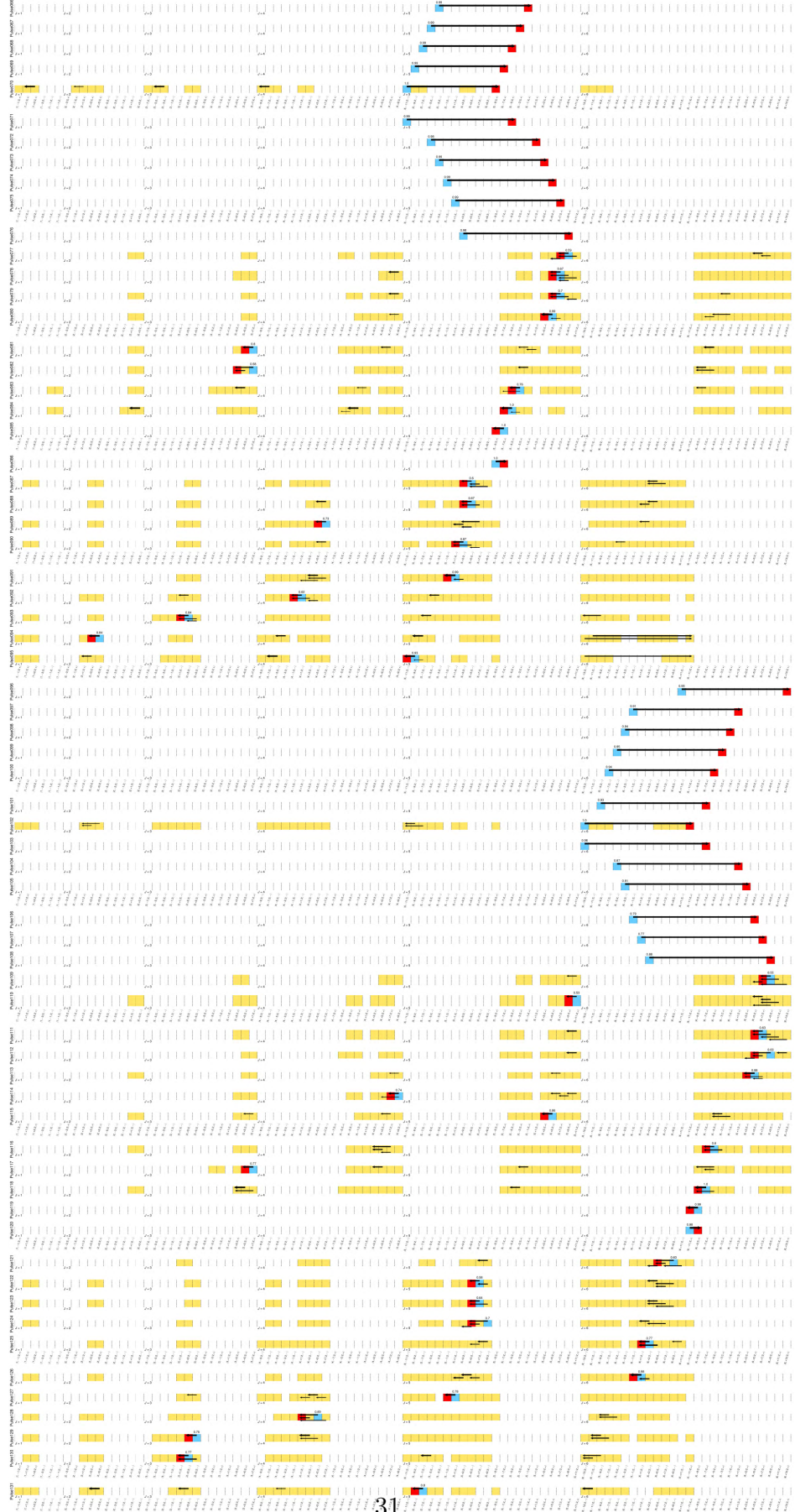


FIG. Extended 9. Pulse library for $J \in \{1, 2, 3, 4, 5, 6\}$ system learning in Fig. 4 (continued, part

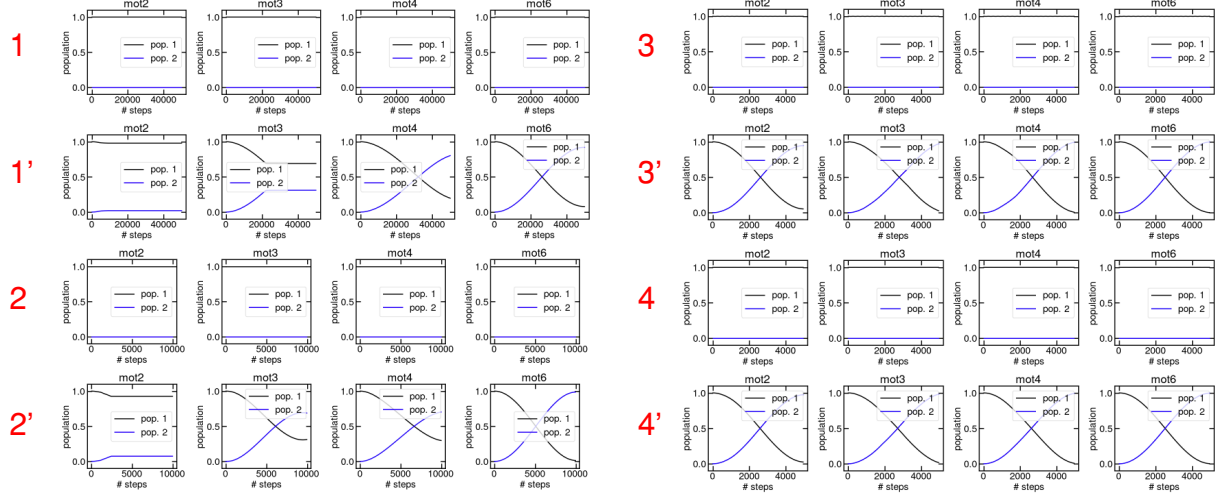


FIG. Extended 10. Time evolution of the populations under the influence of four selected pulses. The four pulses are ordered according to the strength of the Rabi oscillations, with the Rabi rates of 0.19, 0.53, 1.25, and 1.84, respectively, in the unit of 2π kHz. The frequencies of the pulses are set as the energy differences for the transitions (pulse 1: $|2, 5/2, +\rangle \rightarrow |2, 3/2, -\rangle$, 1': $|2, 3/2, -\rangle \rightarrow |2, 5/2, +\rangle$), (pulse 2: $|2, 3/2, +\rangle \rightarrow |2, 1/2, -\rangle$, 2': $|2, 1/2, -\rangle \rightarrow |2, 3/2, +\rangle$), (pulse 3: $|2, -3/2, +\rangle \rightarrow |2, -5/2, -\rangle$, 3': $|2, -5/2, -\rangle \rightarrow |2, -3/2, +\rangle$), (pulse 4: $|2, -3/2, -\rangle \rightarrow |2, -5/2, -\rangle$, 4': $|2, -5/2, -\rangle \rightarrow |2, -3/2, -\rangle$). The Raman pulses are with π (abs.) and σ^- (emit.) polarizations, thus only one direction of the population transfer (namely, those with $\Delta m = 1$) can be driven. The number reported with 'mot' indicates the number of motional manifolds included in the simulations.